Journal of Structural Geology 33 (2011) 1063–1078

Contents lists available at ScienceDirect

Journal of Structural Geology

journal homepage: www.elsevier.com/locate/jsg

Determining the uniqueness of best-fit trishear models

Nestor Cardozo [a,*], Christopher A.-L. Jackson [b], Paul S. Whipp [b,1]

[a] Department of Petroleum Engineering, University of Stavanger, 4036 Stavanger, Norway
[b] Department of Earth Science and Engineering, Imperial College, Prince Consort Road, London SW7 2BP, UK

ARTICLE INFO

Article history:
Received 24 November 2010
Received in revised form
8 April 2011
Accepted 21 April 2011
Available online 29 April 2011

Keywords:
Fault-propagation folding
Trishear
Inverse modeling
Uniqueness

ABSTRACT

We show the application of a simulated annealing algorithm to trishear inverse modeling. The algorithm traverses the parameter space in search for best-fit models without being trapped in local minima, and thus sampling for more possible solutions globally. Simulated annealing is a robust and efficient technique to determine the uniqueness of best-fit trishear models; the spread of possible trishear models that can fit a structure. We first apply the algorithm to a decameter-size, contractional fault-propagation fold in west-central Taiwan, for which there is an exceptional exposure of pre-growth and growth strata. Simulated annealing shows that even for this complete fold dataset with low uncertainties, there is a range of models and fault slip/uplift histories that can fit the data, with the consequent implications for the assessment of seismic hazard. We then apply the algorithm to a kilometer-size, extensional fault-propagation fold, the Hadahid monocline, Gulf of Suez Rift, Egypt. In this monocline there is only surface coverage in the footwall anticline areas and the algorithm was used to delimit the range of possible models that can fit the data and their uncertainties, thus avoiding biases in the interpretation. Simulated annealing suggests that the along-strike structural variability of the monocline can result from along-strike variability in fault slip, fault propagation to fault slip ratio and depth of fault nucleation. Both examples illustrate the benefits of searching for a possible range of models rather than a precise best-fit model when modeling fault-propagation folds. In an attempt to understand which parameters control fault development, and also how the spread of possible solutions varies with fold growth, we apply the algorithm to four sequential stages of a published, analog clay model of an extensional forced fold. The inversions of the natural examples and the analog model suggest that the spread of the possible models is a manifestation of the data uncertainties, the suitability of the trishear model, fold evolution, and rock mechanical properties.

1. Introduction

Subsurface (e.g. Shaw and Shearer, 1999; Corfield and Sharp, 2000), field (e.g. Erslev and Mayborn, 1997; Ferrill et al., 2005), and modeling studies (e.g. Withjack et al., 1990; Finch et al., 2003, 2004) have demonstrated that fault-propagation folding is an important deformation process during the early stages of fault growth in extensional and contractional settings. These studies have indicated that the geometry and evolution of fault-propagation folds are controlled by the interplay of various factors including the dip of the underlying fault and the depth of the fault tip at the initiation of fault propagation, the ratio of fault propagation to fault slip, and the extent of folding around the propagating fault tip. However, it is difficult to deduce these parameters in the field or subsurface, in part due to limited exposures and resolution respectively. Thus, to understand the range and relative importance of these parameters, various modeling approaches have been utilized. In particular, in the last decades, several studies have shown the application of trishear kinematic modeling (Erslev, 1991; Allmendinger, 1998) to fault-propagation folding. Trishear has been used to predict the finite strain and fracturing of fault-propagation folds (e.g. Allmendinger et al., 2004; Cardozo et al., 2005), the growth strata geometries associated with these structures (e.g. Hardy and Ford, 1997; Gawthorpe and Hardy, 2002), and the seismic hazard posed by underlying blind faults (e.g. Allmendinger and Shaw, 2000; Champion et al., 2001).

Trishear modeling of natural examples of fault-propagation folds, however, presents a fundamental problem, as trishear is an incremental rather than a graphical model and there are no mathematical or geometrical rules to relate the model parameters to the fold geometry. This difficulty can be solved by formulating trishear modeling as an inverse problem whereby within a group of

* Corresponding author. Tel.: +47 5558 3693.
E-mail addresses: nfcd@mac.com, nestor.cardozo@uis.no (N. Cardozo).
[1] Present address: Statoil ASA, Sandsliveien, Postboks 7200, 5020 Bergen, Norway.

0191-8141/$ – see front matter © 2011 Elsevier Ltd. All rights reserved.
doi:10.1016/j.jsg.2011.04.001

trishear models, one searches for the model that best restores a folded bed to a straight line in 2D or plane in 3D (Allmendinger, 1998; Cardozo and Aanonsen, 2009), or the model that best deforms beds to reproduce their intersections along a profile (Cardozo, 2005). The success of a particular model in restoring or deforming bedding data is evaluated through an objective function (f_{obj}). The aim of the inversion is to find the model with the lowest f_{obj}; this model is known as the best-fit model (Cardozo and Aanonsen, 2009).

Traditionally, the best-fit model is found through a "brute force", grid-search based approach. Using this approach, every model within a search matrix is evaluated and the model with the lowest f_{obj} is chosen (Allmendinger, 1998). This method is robust (it is not affected by local minima) but inefficient. Recent application of gradient-based optimization algorithms to the trishear inverse problem by Cardozo and Aanonsen (2009) has resulted in faster inversions. From an initial estimate, these algorithms traverse the parameter space in search of an f_{obj} minimum, thus considerably reducing the time needed to undertake the inversion. Gradient-based optimization algorithms, however, are affected by local minima (Cardozo and Aanonsen, 2009).

Given the limitation of these different modeling approaches, it is difficult to evaluate the uniqueness of best-fit trishear models and to assess if there are any other models (i.e. additional local minima), besides the best-fit model, that can fit equally well the data. Grid-search techniques are designed to provide one solution corresponding to a global f_{obj} minimum. f_{obj} values of the tested models can be contoured to visualize local minima (e.g. Allmendinger et al., 2004), but practical constraints on the limits and step size of the searched parameters can result in the algorithm not sampling all local minima. Gradient-based optimization algorithms are trapped in local minima, and the only way to sample for possible solutions is running several searches from different initial estimates spread throughout the parameter space (Cardozo and Aanonsen, 2009). However, this has practical limitations associated to the maximum possible number of searches, and there is no guarantee that this strategy will sample all local minima even if the initial estimates are closely spaced and regularly distributed. Therefore, we lack a numerical tool to assess the uniqueness of trishear models. This is an issue in the modeling of fault-propagation folds, where often data coverage is limited (e.g. less data in steeply-dipping regions), and the parameters controlling fold geometry (e.g. geometry and slip of underlying fault) are poorly constrained.

In this paper, we apply a more robust simulated annealing algorithm to trishear inverse modeling. In comparison to gradient-based optimization algorithms, simulated annealing is similarly efficient and is not affected as much by local minima. In addition, the algorithm is able to explore globally the parameter space for possible solutions, providing a quantitative assessment of the uniqueness of best-fit trishear models. We show the application of the algorithm to a contractional fault-propagation fold in west-central Taiwan, for which there is an exceptional exposure of pre-growth and growth strata (Lin et al., 2007). Modeling of the fold shows that there is a range of trishear models and fault slip histories that can fit the structure, with the consequent implications for the assessment of seismic hazard. We then apply the algorithm to an extensional fault-propagation fold in western Sinai, Egypt; the Hadahid monocline (Whipp, 2011). In this case, bedding intersections are well exposed in the footwall, but there are no data constraining the geometry of the hanging wall or the underlying master fault. Application of the algorithm to this example provides a framework within which to evaluate the possible fault-propagation folding scenarios that might fit the available data. Finally, we apply the algorithm to four sequential stages of an analog clay model of an extensional forced fold by Withjack et al. (1990). This gives some indications about the trishear parameters that control fold development, as well as the variation in the spread of possible solutions with fold growth. These three examples show the versatility of the simulated annealing algorithm, and highlight the importance of defining a range of models rather than a unique model when investigating the controls on the development of fault-propagation folds in both contractional and extensional settings.

2. Methodology

Trishear is a kinematic model of fault-propagation folding in which the slip discontinuity on a fault is distributed into a triangular zone of shear radiating from the propagating fault tip (Erslev, 1991; Allmendinger, 1998). In 2D, trishear deformation results from the combination of six parameters linked to the geometry and propagation history of the fault (Allmendinger, 1998; Fig. 1a): (i) fault-tip location (x and y), (ii) fault dip (ramp angle), (iii) fault propagation to fault slip ratio (P/S), (iv) apical angle of the triangular zone or trishear angle (TA), and (v) fault slip. In 3D, and assuming a simple linear variation of P/S, TA and fault slip along the fault tipline, the number of parameters increases to fourteen (Cardozo, 2008). The basic problem in trishear modeling of natural structures (i.e. trishear inverse modeling) is to determine the combination of parameters that best fits a folded profile in 2D or surface in 3D. As stated in the introduction, this is an inverse problem where, within a group of models, we search for the model with the lowest f_{obj} or best fit (Cardozo and Aanonsen, 2009).

In this paper, we solve this problem using an optimized trishear inverse modeling strategy similar to the employed by Cardozo and Aanonsen (2009), with the only difference being that we apply a more robust simulated annealing algorithm to the inversion. Simulated annealing is an optimization method that models the process of heating a material and then slowly lowering the temperature to minimize the system energy. The simulated annealing algorithm we use is from the MATLAB Global Optimization Toolbox™ and is called "simulannealbnd" (The MathWorks Inc., 2010). Similar to the gradient-based optimization algorithms used by Cardozo and Aanonsen (2009), simulannealbnd traverses the parameter space from an initial estimate in search of an f_{obj} minimum. During each iteration, a new point in the parameter space is randomly generated. The distance of the new point from the current point, or the extent of the search, is controlled by the temperature. The algorithm accepts points that lower the value of f_{obj}, but contrary to the simpler gradient-based optimization algorithms, it can also accept with a certain probability (controlled by the temperature) points that raise f_{obj}. By accepting worse solutions, simulannealbnd avoids being trapped in local minima, and is able to explore globally for more possible solutions. An annealing schedule is selected to systematically decrease the temperature. As the temperature decreases, the extent of the search decreases. Reannealing (raising the temperature) is applied after a certain number of iterations to avoid getting caught at local minima. simulannealbnd can be used to solve unconstrained (i.e. no limits on the searched parameters) or constrained (i.e. explicit limits on the searched parameters) optimization problems. In the examples presented in this paper, we limit the extent of the searched trishear parameters and use the constrained version of the algorithm. All the examples in the paper are in two dimensions, and the trishear models follow the simplest, linear v_x field for a symmetric trishear zone (Zehnder and Allmendinger, 2000). However, it is straightforward to extend our methodology to three dimensions and/or more complex velocity fields.

To illustrate the general performance of the algorithm, we applied it to the contractional, forward trishear model of Fig. 1a. The parameters responsible for the formation of the fold are shown in the first column of the table shown in Fig. 1a. Modeling of

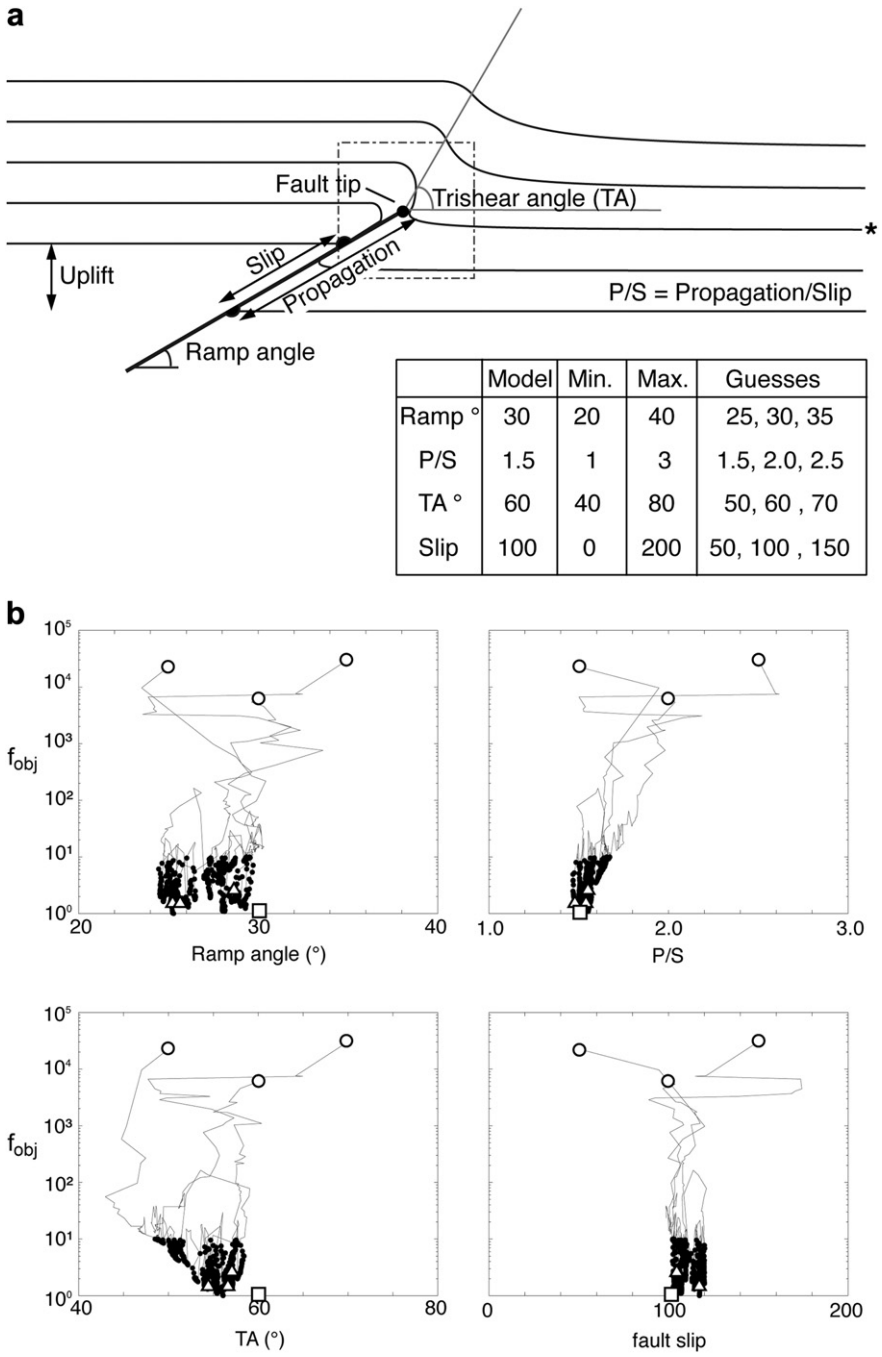

	Model	Min.	Max.	Guesses
Ramp °	30	20	40	25, 30, 35
P/S	1.5	1	3	1.5, 2.0, 2.5
TA °	60	40	80	50, 60 , 70
Slip	100	0	200	50, 100 , 150

Fig. 1. a. Parameters of the trishear model in two-dimensions. Hanging wall uplift is the variable plotted in the ordinate of Fig. 5b. Model parameters and minimum, maximum, and guess values for the inversions in b are shown in the table. Dashed rectangle shows the area where the fault tip was searched. b. Simulated annealing inversions of the bed marked with an asterisk in a. Three inversions are included and their paths are shown on: Ramp angle versus f_{obj}, P/S versus f_{obj}, TA versus f_{obj}, and fault slip versus f_{obj} diagrams. A total of 20,000 iterations were used in each inversion. In each plot, the circle represents the initial estimate, and the triangle the final iteration. Black dots indicate models with $f_{obj} \leq 10$. Squares indicate the parameter values of the synthetic model. Notice that the vertical f_{obj} axis is logarithmic.

a synthetic fold, such as that shown in Fig. 1a, might seem circular, but is the only situation for which we can evaluate with complete confidence the success of the algorithm. We searched for the combination of the six trishear-parameters (i.e. the model) that best restores bed 3 (marked by a '*' in Fig. 1a) using the maximum, minimum and guess parameter values described in this figure. Even though we are dealing with a synthetic model, this case is complicated because the parameter space has several local minima, to the point that gradient-based optimization algorithms do not perform well (Cardozo and Aanonsen, 2009). Three simulated annealing inversions were run, each one starting at a different location in the parameter space, and consisting of 20,000 iterations. Fig. 1b shows the results of the inversions. There are a range of low f_{obj} models (black dots in Fig. 1b) that fit well the bed. These "possible" models have P/S and fault slip values that are close to those of the synthetic model (squares in Fig. 1b), while their ramp angle and TA are less well constrained (Fig. 1b). For a bed with 500 points, each inversion takes about 5 min in a standard personal

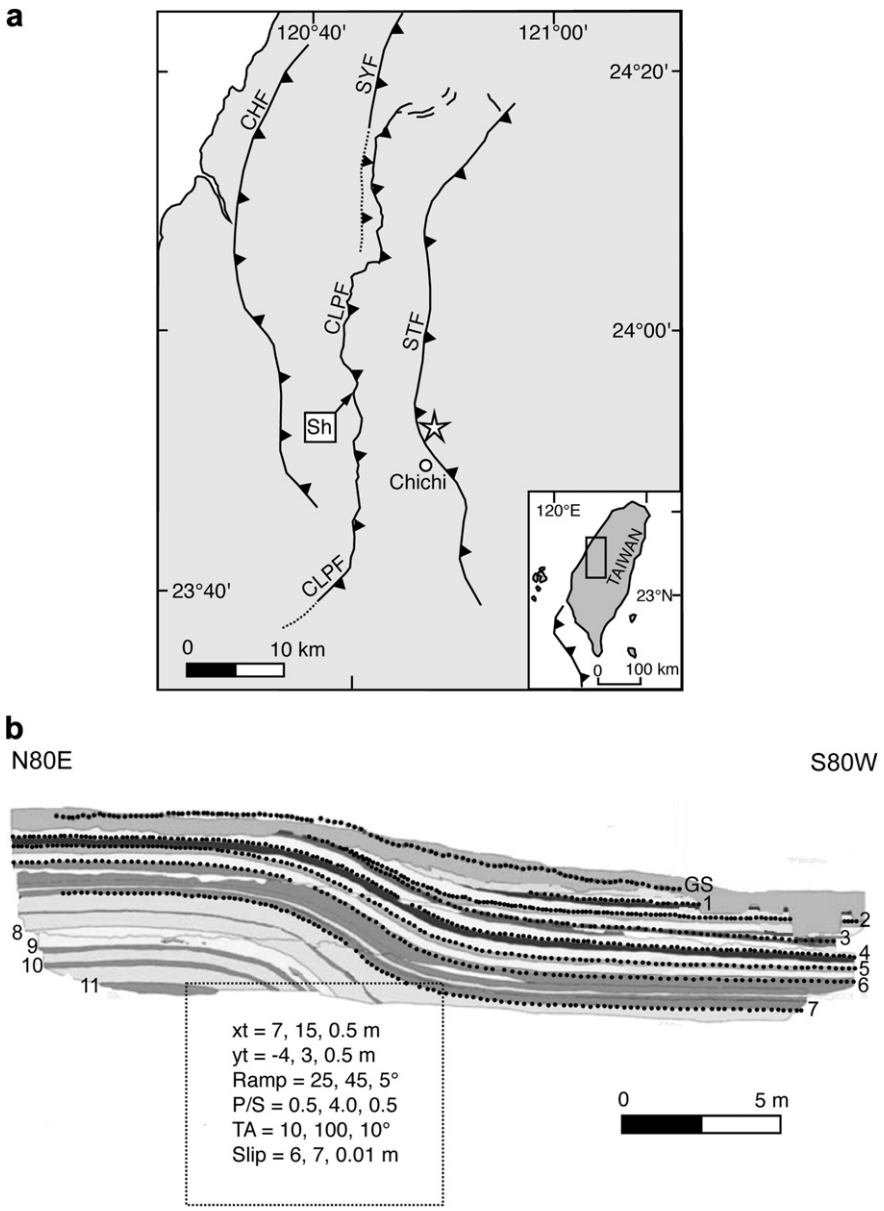

Fig. 2. a. Geological setting and location of the Shijia trench site (Sh) in west-central Taiwan. From the western deformation front, the major thrust faults are: Changhua fault (CHF), Sanyi fault (SYF), Chelungpu fault (CLPF), and Shuangtung fault (STF). Star is the epicenter of the 1999 Chichi earthquake. Modified from Chen et al. (2007a). b. Geometry of the strata in the Shijia trench. Beds 11 to 5 are pre-growth, and 4 to GS are growth. Dotted beds 7 to GS are the ones used in this paper. Beds numbering scheme is similar to Lin et al. (2007). Dotted rectangle and text inside indicate the parameter ranges and step sizes selected by Lin et al. (2007) for grid-search, trishear inverse modeling of the structure. Dotted rectangle shows the area where the fault tip was searched. For each parameter, the entries correspond to minimum limit, maximum limit, and step-size respectively. Modified from Lin et al. (2007).

computer. The running times of all the inversions discussed in this paper are in the order of minutes.

3. Application to natural examples

To show the application of the algorithm to natural examples, we selected two fault-propagation folds: one from a contractional (Shijia trench site, Section 3.1), and one from an extensional (Hadahid monocline, Section 3.2) setting. The first example is a superb, decameter-size exposure of a trishear-like contractional fault-propagation fold reactivated during the 1999 Chichi earthquake in west-central Taiwan (Lin et al., 2007). In this case, pre-growth and growth strata can be clearly traced across the structure without significant errors on their locations. The purpose of using this example is to show that, even for an exceptionally well-exposed fault-propagation fold, there can be ambiguity in the selection of the best-fit model and it is important, therefore, to determine the uniqueness of a solution. The second example is a kilometer-size extensional fault-propagation fold in western Sinai; in this example the footwall is well-exposed, but the hanging wall and underlying master fault are not exposed (Whipp, 2011). This situation is the rule rather than the exception when modeling natural fault-propagation folds; data are often restricted to a window of limited spatial extent in the field, or structural geometries are poorly imaged in seismic datasets in the subsurface.

3.1. Shijia trench site, Chelungpu fault, Taiwan

The Shijia trench site is located in the southern segment of the Chelungpu fault in west-central Taiwan (Fig. 2a). The Chelungpu fault is the second major thrust eastward from the western deformation front (Fig. 2a, Yue et al., 2005). The fault was reactivated during the 1999 Chichi earthquake (M_W 7.6), which had a shallow depth of about 8 km. The fault had a surface rupture exceeding 100 km and surface uplifts ranging from 2 to 10 m (Chen et al., 2001). This severe earthquake resulted in 2500 fatalities and significant loss of property. Most of the coseismic Chichi scarps are *fault* scarps that formed when the fault reached the surface. However, there are also *fold* scarps formed by distributed deformation ahead of a blind thrust tip. The scarp at the Shijia trench site is a fold scarp (Chen et al., 2007a).

The trench is normal to the fold scarp and it has a length of 27 m and a depth of 7 m (Lin et al., 2007; Fig. 2b). The sediments in the trench are relatively young and not compacted, and can be divided based on eleven sand and clay layer boundaries (1–11 in Fig. 2b, Lin et al., 2007). Detailed description of these strata is given by Chen et al. (2007b) and Lin et al. (2007). The beds are folded across the trench, and show a trishear-like geometry with rounded anticlinal fold hinges and downward steepening forelimbs (Fig. 2b). Beds below layer boundary 5 have fairly uniform thickness outside the folded zone and are considered to be pre-growth strata. Beds above layer boundary 5 thin and pinch out toward the fold scarp, suggesting that they represent syngrowth strata (Fig. 2b). These syngrowth beds were deposited during interseismic periods and folded during earthquake events (Lin et al., 2007; Chen et al., 2007b). The geometry of the underlying fault is constrained by two shallow boreholes (Lin et al., 2007, their Fig. 6). Shear zone deformation fabrics and the juxtaposition of older Pliocene sediments over much younger gravel beds in the boreholes indicate that the underlying fault have possible dips of 25–35° or 45–50° E, and that the fault tip is within the area shown by the dotted rectangle in Fig. 2b (Lin et al., 2007).

Lin et al. (2007) used trishear inverse modeling to infer the deformation history of the fold scarp. Their methodology consisted of two steps: first, they inverted for the trishear parameters (fault tip location, ramp angle, P/S, TA, and fault slip) that best restore the pre-growth strata (beds 5 to 11 in Fig. 2b) to straight lines. For this, they used a grid-search strategy with ranges and parameters step sizes as shown in Fig. 2b. The best-fit ramp angle, P/S, TA and fault slip from the grid-search inversion of the pre-growth strata are 35°, 2.5, 80° and 6.45 m, respectively (Fig. 3a). The estimated fault slip is the cumulative of the earthquake events that formed the fold scarp. Second, they assumed the ramp angle, P/S and TA to be constant throughout the deformation, and inverted for the fault slip that best restores each one of the growth strata (beds 4 to GS in Fig. 2b) using a grid-search strategy. This allowed the estimation of the earthquake events that formed the scarp (Fig. 3b). The history of deformation thus derived from trishear inverse modeling (Fig. 3b) is complementary to that obtained by trench investigation (Chen et al., 2007b), and the inferred slip by the Chichi earthquake (4.37 m, Fig. 3b) is similar to that measured in a GPS station 2 km east of the trench (3.38 m, Lin et al., 2007). However, is Fig. 3b the only model that could reproduce the fold? Are there any models (i.e. fault slip histories) that could explain equally well the data? Since the amount of fault slip is a proxy for earthquake magnitude,

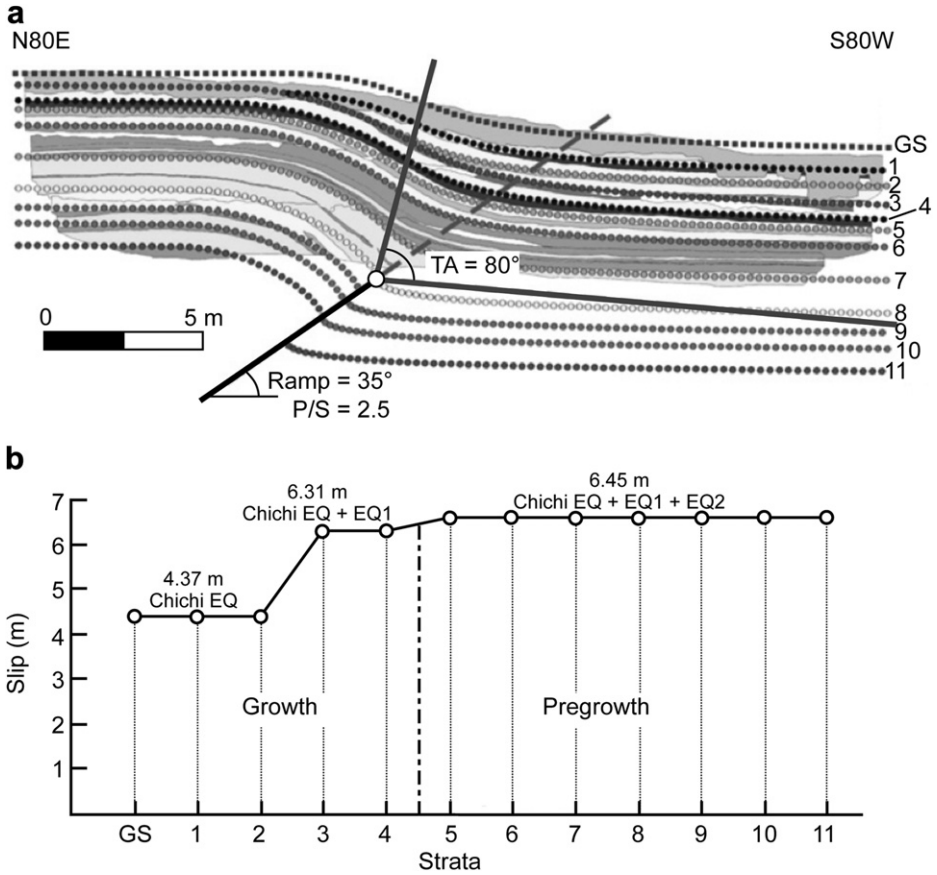

Fig. 3. a. Comparison of best-fit trishear model of Lin et al. (2007) with the strata in the Shijia trench site. The best-fit model matches the pre-growth (beds 5 to 11) and growth (beds 4 to GS) strata. b. Fault slip history suggested by best-fit trishear model and restoration of the growth strata. Modified from Lin et al. (2007).

evaluating the uniqueness of the best-fit model has important implications for the assessment of seismic hazard in the area.

To address this question, we follow the methodology of Lin et al. (2007), but this time we apply the simulated annealing algorithm to the inversion. We use the most continuous pre-growth strata in the trench (beds 5, 6 and 7, Fig. 2b) and invert for the trishear parameters that best restore these beds. We set the lower limit of the search ($\mathbf{a_{min}}$) to [7 m, −4 m, 25°, 1.0, 20°, 5 m] (x and y location of fault tip, ramp angle, P/S, TA, and fault slip), the upper limit ($\mathbf{a_{max}}$) to [15 m, 3 m, 45°, 4.0, 100°, 10 m], and the initial estimate ($\mathbf{a_0}$) to [11 m, −0.5 m, 35°, 2.5, 60°, 7.5 m], which is halfway between $\mathbf{a_{min}}$ and $\mathbf{a_{max}}$. The limits $\mathbf{a_{min}}$ and $\mathbf{a_{max}}$ are similar to those used by Lin et al. (2007, Fig. 2b), except that we use a broader range for fault slip (5–10 m). Contrary to the grid-search method where the parameters step sizes are prescribed by the user (Fig. 2b), in the simulated annealing algorithm the parameters step sizes are variable and are defined by the temperature. This allows us sampling of the parameter space at different resolutions, effectively zooming in (when the temperature decreases) and out (when reannealing is applied) of the parameter space. Practical limitations (e.g. maximum number of trial models), which forced Lin et al. (2007) to use parameter step sizes possibly too coarse to identify all local minima (Fig. 2b), are not present in our analysis.

Fig. 4 shows the results of the simulated annealing inversions for the trishear parameters that best restore pre-growth beds 5 (Fig. 4a), 6 (Fig. 4b), and 7 (Fig. 4c). The paths of the optimizations are shown for four of the parameters of the inversion: ramp angle, P/S, TA, and fault slip. A total of 2000 iterations were used in the inversion of each bed. Fig. 4 illustrates the evolution of the search from the initial estimate (circles) to the final iteration (triangles). During this evolution, which comprises several cycles of temperature reduction and increase, the algorithm identified several local minima (black dots in Fig. 4). These are trishear models that can replicate the pre-growth bedding data. The ramp angle of these "possible" models is either "low" (25–30°. Beds 5, 6 and 7), "intermediate" (35°. Beds 5 and 7) or "high" (40°. Beds 5 and 6, Fig. 4). The P/S varies less, with possible values ranging between 2.0 and 3.0 and most of the local minima around 2.5 (Fig. 4). The range of possible TA is quite broad, with values ranging between 40 and 90° (Fig. 4). Finally, the fault slip is either "low" (6–7 m. Beds 5 and 6), "intermediate" (7.5–8 m. Bed 7) or "high" (9–10 m. Beds 5 and 6, Fig. 4).

Any of the models indicated by the black dots in Fig. 4 fits well the pre-growth bedding data (beds 5 to 7, Fig. 2b). We use these models (about 1000) to invert for the fault slips that best restore the growth strata (beds 4 to GS, Fig. 2b). Essentially, we use the fault tip location, ramp angle, P/S and TA of each of the possible models, and search for the fault slips that best restore the growth strata using the simulated annealing algorithm. In this analysis, we choose not to use bed 1 (Fig. 2b) because it has short extent across the studied section and accordingly appears to give spurious results. In addition, we rejected models that suggested decreasing cumulative fault slip with time. The results of the growth strata inversions are summarized in Fig. 5. A total of 146 fault slip models fit the growth strata. These models have lower and, in their majority, higher fault

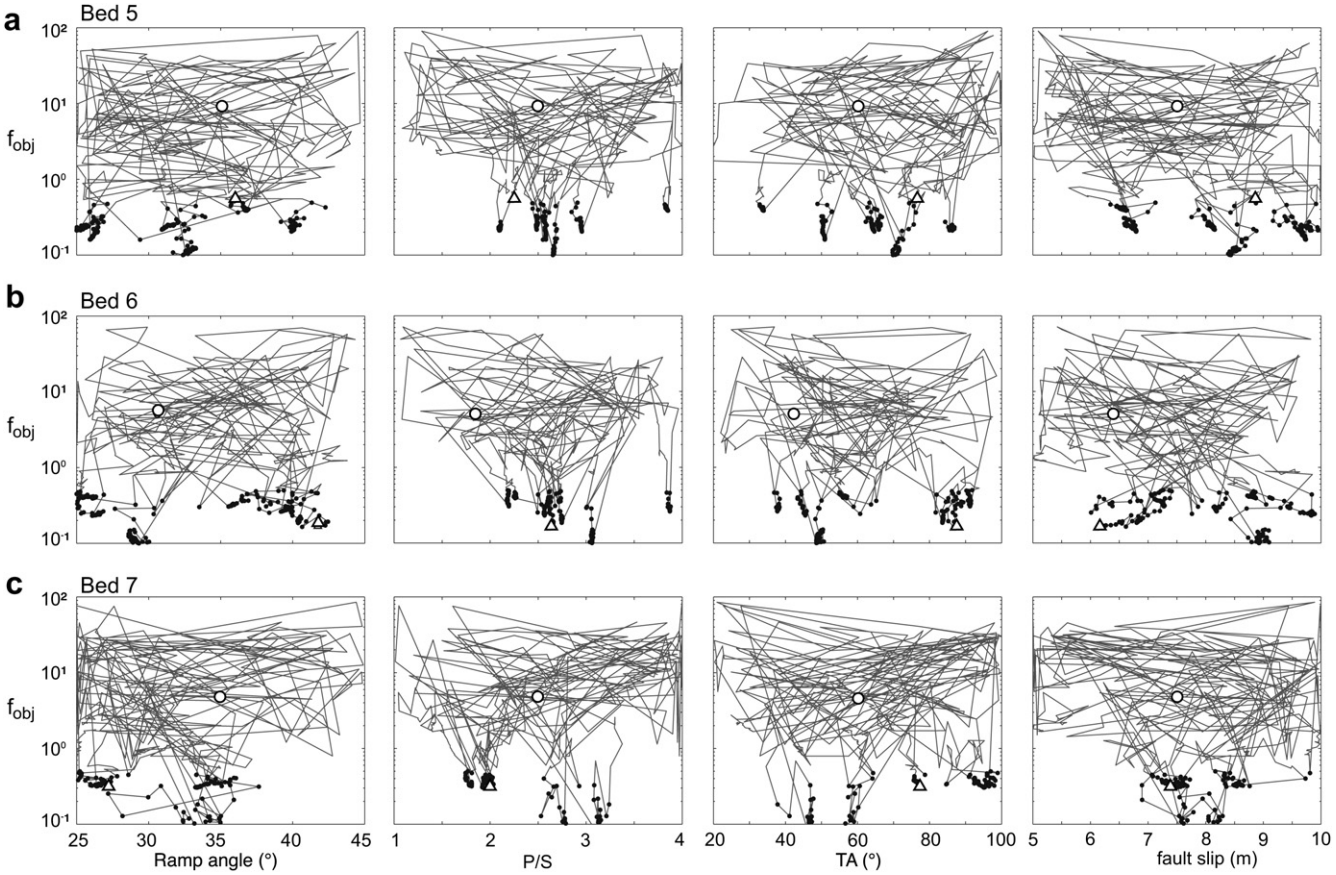

Fig. 4. Evolution of simulated annealing optimizations for the trishear parameters that best restore a. Bed 5, b. Bed 6, and c. Bed 7 of Fig. 2b. The paths of the optimizations are shown on: Ramp angle versus f_{obj} (first column), P/S versus f_{obj} (second column), TA versus f_{obj} (third column), and fault slip versus f_{obj} (fourth column) diagrams. A total of 2000 iterations were used in each optimization. In each plot, the circle represents the initial estimate, and the triangle the final iteration. Black dots indicate models with $f_{obj} \leq 0.5$. Notice that the vertical f_{obj} axis is logarithmic.

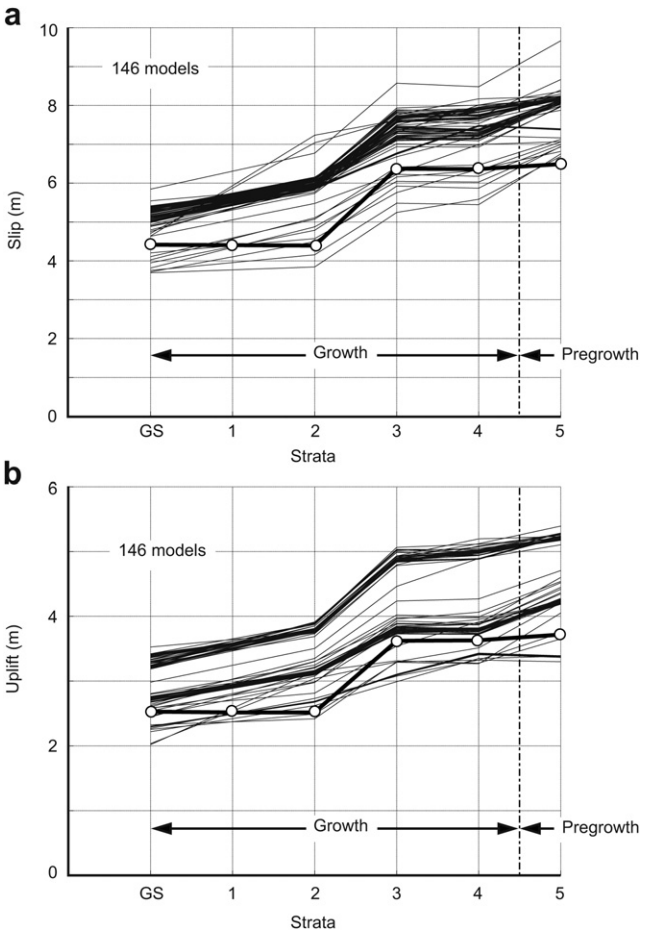

Fig. 5. a. Fault slip, and b. Hanging wall uplift histories of the models that fit well the Shijia trench, pre-growth and growth strata. In a and b, heavy line with circles is the history of fault slip/uplift suggested by Lin et al. (2007).

slips than the best-fit model of Lin et al. (2007) (i.e. thick line with circles in Fig. 5a). The models suggest that the fault slip associated with the 1999 Chichi earthquake was between 3.7 and 5.8 m, with most of the models (about 120) having fault slip between 5 and 5.5 m (Fig. 5a); these values are higher than the fault slip measured in a GPS station 2 km east of the trench (3.38 m, Lin et al., 2007). Interestingly, as proposed by the best-fit model of Lin et al. (2007, Fig. 3a), most of the models suggest one earthquake event between deposition of beds 2 and 3, and another earthquake between beds 4 and 5 (Fig. 5a). The fault slip associated with the earthquake between beds 2 and 3 is between 0.8 and 1.8 m, with half of the models having fault slip greater than 1.6 m (Fig. 5a). These values are in agreement with the fault slip estimated by Lin et al. (2007) for the same earthquake (1.9 m, Fig. 3b). The fault slip by the earthquake between beds 4 and 5 is between 0 and 1.3 m, with about one third of the models having fault slip greater than 0.8 m, and most of the rest of the models having low fault slip of 0.2–0.3 m (Fig. 5a). These values are higher than the fault slip estimated by Lin et al. (2007) for the same earthquake (0.14 m, Fig. 3b). In addition, most of the models suggest an earthquake between the present (GS in Fig. 2b) and bed 2. The inferred fault slip by this earthquake ranges between 0.1 and 1.4 m, with the majority of the models (about 100) having fault slip between 0.7 and 1.0 m (Fig. 5a). This earthquake was not identified by the trishear inverse modeling of Lin et al. (2007, Fig. 3b), although it was identified through trench investigation (Chen et al., 2007b; Lin et al., 2007, their Table 2).

A clearer picture of the distribution of the possible fault slip models can be obtained by plotting the hanging wall uplift (Fig. 1a) of the models (Fig. 5b). In this case, three main groups of models can be distinguished: Low (about 38), intermediate (about 46), and high (about 62) uplift models, which have lower, similar, and higher uplift than the model of Lin et al. (2007), respectively. Further inspection of the intermediate uplift models show that a few models (about 5) have a relatively low ramp angle of 26°, and the rest of the models (about 40) have higher ramp angles between 31 and 34°. Fig. 6 shows examples of these model groups. All model groups (black lines) fit the bedding data (red dots). A significant difference between the models is the geometry of the restored strata (gray lines in Fig. 6), with low uplift models predicting an average dip of the restored strata of 0.5°W (Fig. 6a), intermediate uplift models of 1.0 (Fig. 6b) to 1.2°E (Fig. 6c), and high uplift models of 2.5°E (Fig. 6d). Of all the model groups, the high uplift model group (Fig. 6d), which has very high P/S and narrow TA (3.87 and 38° respectively), is perhaps the only one that can be ruled out, as it predicts uplift by the 1999 Chichi earthquake of 3.2–3.4 m, which is much higher than the 2.15 m uplift measured in a nearby GPS station (Lin et al., 2007), and it suggests a restored bedding dip of 2.5°E which is too high. Any of the remaining low or intermediate uplift models (Fig. 6a–c) are a good representation of the trench bedding data and are within the constraints imposed by borehole data on fault geometry, and GPS data on the slip/uplift by the Chichi earthquake (Lin et al., 2007). The intermediate uplift with high ramp angle (34°) model group (Fig. 6c) is similar to the model of Lin et al. (2007, Fig. 3a), but as our analysis suggests, it is not the only model that can fit the trench data. Lower ramp angle (26°) models with low (Fig. 6a) or intermediate uplift (Fig. 6b) can also explain the trench data. In summary, rather than a single model, a range of trishear models with their corresponding fault slip/uplift histories and related seismic hazard can fit the trench data. These models plot within the low to intermediate uplift areas of Fig. 5b.

3.2. Hadahid monocline, Gulf of Suez Rift, Egypt

The Hadahid Fault System (HFS) is located on the eastern margin of the Suez Rift, Western Sinai, Egypt (Fig. 7). This 30 km long, NW–SE trending, W–SW dipping normal fault system define the southwestern margin of the El Qaa fault block, at the southern end of the Suez Rift central dip province (Moustafa and El-Raey, 1993; Sharp et al., 2000). The rift developed during the Late Oligocene to Early Miocene and its stratigraphy consists of three megasequences: (i) A pre-rift Cambrian to Lower Cretaceous clastic-dominated succession (Nubian Sandstones), (ii) a pre-rift Mesozoic (Raha, Wata, Matulla and Sudr formations) to Early Tertiary (Esna, Thebes, Darat and Mokattam formations) mixed carbonate-clastic succession, with marked competence contrast existing between ductile mudstone-dominated (Duwi, Esna and Darat formations) and brittle carbonate-sandstone units, and (iii) an Oligocene-Miocene succession of syn-rift (the clastic-dominated Gharandal Group) and post-rift strata (evaporites of the Ras Malaab Group) (Moustafa, 1987; Patton et al., 1994; Sharp et al., 2000).

In the south, the HFS splays off from the rift-bounding Sinai Massif and Gebah faults (Fig. 7). At this locality, the majority of displacement on the rift-border fault system (ca. 4 km) is transferred onto the HFS (ca. 2.5 km) (e.g. Moustafa and El-Raey, 1993; Sharp et al., 2000). In general, fault displacement decreases northwestwards along the HFS, with a surface-breaking fault and breached monocline in the south being replaced by an unbreached monocline above a blind fault tip to the north (Whipp, 2011; Fig. 7). The monocline consists of an asymmetric footwall anticline-hanging wall syncline pair; both sharing a steep limb with increased bedding dips toward the HFS. This geometry is interpreted as an

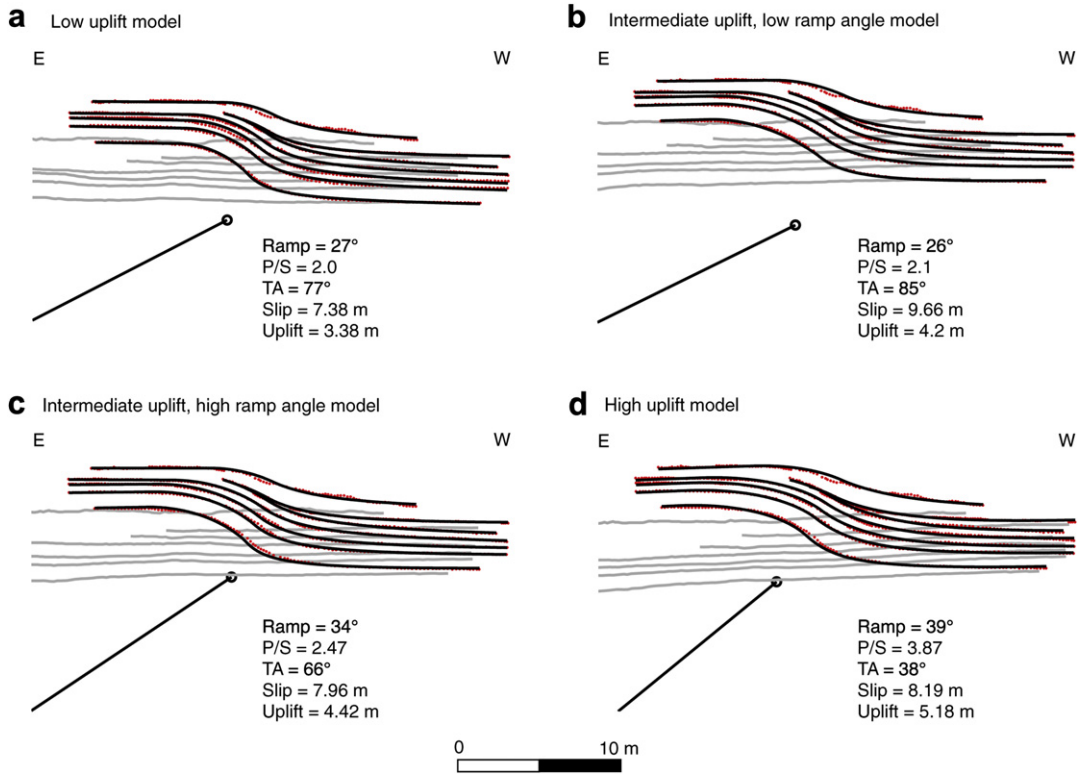

Fig. 6. Examples of trishear models that can fit the Shijia trench, pre-growth and growth strata. a. Low uplift model, b. Intermediate uplift with low ramp angle model, c. Intermediate uplift with high ramp angle model, and d. High uplift model. In all cases, the red dots are the bedding data, the black lines are the trishear model, and the gray lines are the restored strata. Notice that all four trishear models fit the bedding data. (For interpretation of the references to color in this figure legend, the reader is referred to the web version of this article.)

extensional fault-propagation fold formed ahead of the upper tipline of the upwardly-propagating HFS (Whipp, 2011; Hardy and McClay, 1999). The HFS consists of eight fault-fold segments, each ca. 3–7 km in length (Whipp, 2011). In this paper, we focus on the four northernmost segments, mainly the Ratamat segment (section 5), the Hadahid monocline segment (sections 3 and 4), the Hadahid fault segment (section 2), and the Feiran segment (section 1, Fig. 7).

Detailed surface geological mapping (1:2000 and 1:5000. Whipp, 2011) and topographic data (90 m DEM), allow us to construct topographic profiles with key bedding intersections (i.e. stratigraphic contacts) across the studied fault-fold segments of the HFS (Fig. 8). In the sections where the monocline is breached (sections 2, 3 and 5 in Fig. 8), the location of the surface-breaking master fault (i.e. the normal fault system which created the monocline) can be constrained. However, limited vertical exposure does not allow the cross-sectional geometry of the master fault to be constrained at depth. In the sections where the monocline is unbreached (sections 1 and 4 in Fig. 8), although the surface fold geometry is well constrained, exposures are not sufficient to determine the subsurface geometry and tip location of the master fault. In addition, surface exposure is restricted to the footwall anticline and the steep limb of the hanging wall syncline immediately adjacent to the HFS (Fig. 8). There are no available surface or subsurface data to constrain the geometry of the hanging wall syncline west of the HFS. In this section, we use trishear inverse modeling to infer, from the surface data, the geometry of the master fault and associated fold at depth, and to predict parameters such as fault displacement and P/S.

The inverse trishear modeling strategy used in this section is similar to that outlined in Cardozo (2005). In the case of the HFS, neither the fault tip location, nor the ramp angle, nor the amount of fault slip associated with individual fault-fold segments is known. Therefore, we want to search for the combination of all six trishear parameters (x and y fault tip location, ramp angle, P/S, TA, and fault slip) that, from an undeformed layer template, deforms the beds such that their intersections with the selected topographic profile match the observed ones (Fig. 8). This strategy requires the following data (Fig. 8): (i) a topographic profile perpendicular to the strike of the (breached or unbreached) monocline, (ii) key bedding intersections (i.e. stratigraphic contacts) and average bedding dip at each intersection along the profile, and (iii) an undeformed stratigraphic template of the intersected beds in either the footwall or hanging wall. In our case, we set the undeformed template in the footwall. The thickness of pre-rift units used to define the undeformed template represent average stratigraphic thicknesses measured within the study area (Whipp, 2011). Note that in all sections, the beds in the stratigraphic template dip about 10°W (Fig. 8). This is a pre-deformation regional dip related to rotation of major fault blocks along basin bounding faults (Moustafa, 2004) and is not related to the development of the monocline.

From the undeformed stratigraphic template, several forward trishear models were run, each one with a different combination of trishear parameters. For each model, differences in location and dip between the modeled and actual bedding intersections were expressed as an objective function (f_{obj}), similar to that in Cardozo (2005: his Eq. (1)). In the calculation of f_{obj}, bedding intersections on the forelimb area were given five times more weighting than those in the backlimb. This weighting forces the inversion to preferentially fit the forelimb area where folding is more intense and the beds are steeper. In addition, errors in bedding dip were given twice as much weighting as errors in location, to emphasize the importance of this parameter in the inversion. The aim of the

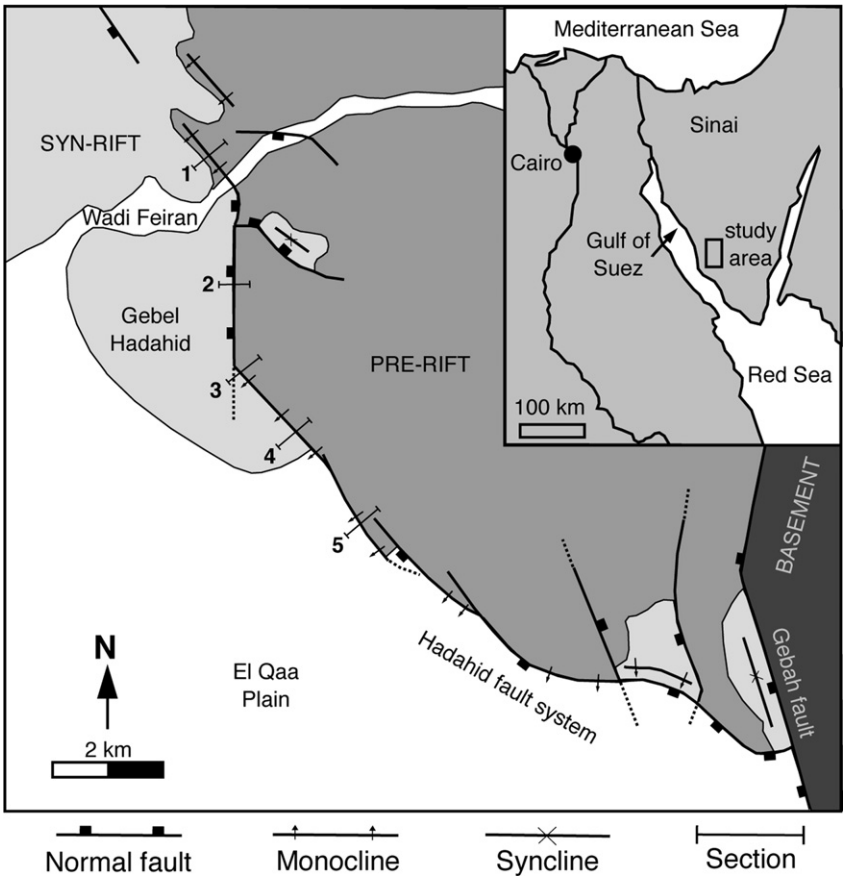

Fig. 7. Simplified geological map of the Hadahid Fault System in Western Sinai, Egypt. The location of sections 1–5 in Fig. 8 are shown.

inversion is to determine the model with the lowest f_{obj}. In this section, we solve this minimization problem using the simulated annealing algorithm. To check the consistency of the solution, four inversions were run for each of the profiles of Fig. 8, each inversion with a different initial estimate of P/S (Table 1). Details about the lower and upper limits, and initial guesses of the inversions are summarized in Table 1.

Fig. 9 shows the results of the simulated annealing inversions for the trishear parameters that best reproduce the bedding intersections along the profiles 1 (Fig. 9a), 2 (Fig. 9b), 3 (Fig. 9c), and 4 (Fig. 9d) of Fig. 8. The paths of the optimizations are shown for four of the parameters of the inversion: ramp angle, P/S, TA, and fault slip. Four inversions (i.e. optimization paths) are shown for each section, each inversion consisting of 750 iterations (initial estimate and final iteration are shown by circles and triangles, respectively. Fig. 9). For each profile, the inversions do not produce a unique solution; different combinations of trishear parameters may fit the profile data (Fig. 9). For this reason, the solution chosen for each profile are referred to as the "selected" model. This model was chosen as the one with low f_{obj} and good visual comparison to the profile data.

Section 1 (Fig. 9a) is in an unbreached segment of the HFS (Figs. 7 and 8a). The inversion of this profile is well constrained with respect to fault slip (150–180 m, Fig. 9a), but not the other trishear parameters. For example, there are a broad range of ramp angles (60–80°), P/S (1.25–2.75), and TA (60–100°) that can fit the profile data (Fig. 9a). A (selected) model with P/S of 1.89 was chosen for section 1 (Table 1, Fig. 10a), mainly because this value is close to that selected for sections 2 and 3 to the south (Fig. 10b–c).

Section 2 (Fig. 9b) is located along a breached segment of the HFS (Figs. 7 and 8b). There are not many bedding intersections in this section, but the inversion has to reproduce the observed surface location of the master fault, and the fact that only the Mokattam Formation (M in Fig. 8) outcrops west of the master fault. Under these circumstances, fault slip is constrained by three of the inversions to be 350–450 m (Fig. 9b), but a range of ramp angles (60–70°), P/S (1.75–2.25), and TA (70–100°) are possible (Fig. 9b). The selected model (Table 1, Fig. 10b) has a P/S of 1.87, similar to section 1, a larger fault slip of 377 m, and a shallower location of the initial fault tip. This model results in breaching of the monocline (Fig. 10b).

Section 3 (Fig. 9c) is also located along a breached segment of the HFS (Figs. 7 and 8c), although here the fault throw is not as high as in section 2. All four searches suggest a fault slip of 350–450 m and low to intermediate fault dip (60–70°, Fig. 9c). Three of the searches suggest a P/S of 1.75–2.0 and a TA of 60–70° (Fig. 9c). This does not, however, rule out possible models with lower P/S (1.25), higher TA (80–100°) and shallower initial fault tips (Fig. 9c). We selected a model with P/S of 1.9 and fault slip of 355 m (Table 1, Fig. 10c). This corresponds to a model in which the final location of the fault tip is close to the present-day surface, and the monocline is almost continuous at the base of the Darat Formation (Fig. 10c). These two relations are observed in the field (Whipp, 2011).

Section 4 (Fig. 9d) is located along an unbreached segment of the HFS (Figs. 7 and 8d). In this profile, the four searches suggest a steeply-dipping fault plane (75–78°). Three of the searches with the lowest f_{obj} favor a model with low P/S (1.4), intermediate TA (60°), and fault slip of 375–425 m (Fig. 9d). The selected model has a P/S of 1.43 and fault slip of 416 m (Table 1, Fig. 10d). Models with P/S and fault slip values close to these are the only ones that fit the profile data.

Section 5 is located along a segment of the HFS which is locally breached (i.e. footwall anticline-hanging wall syncline fold pair)

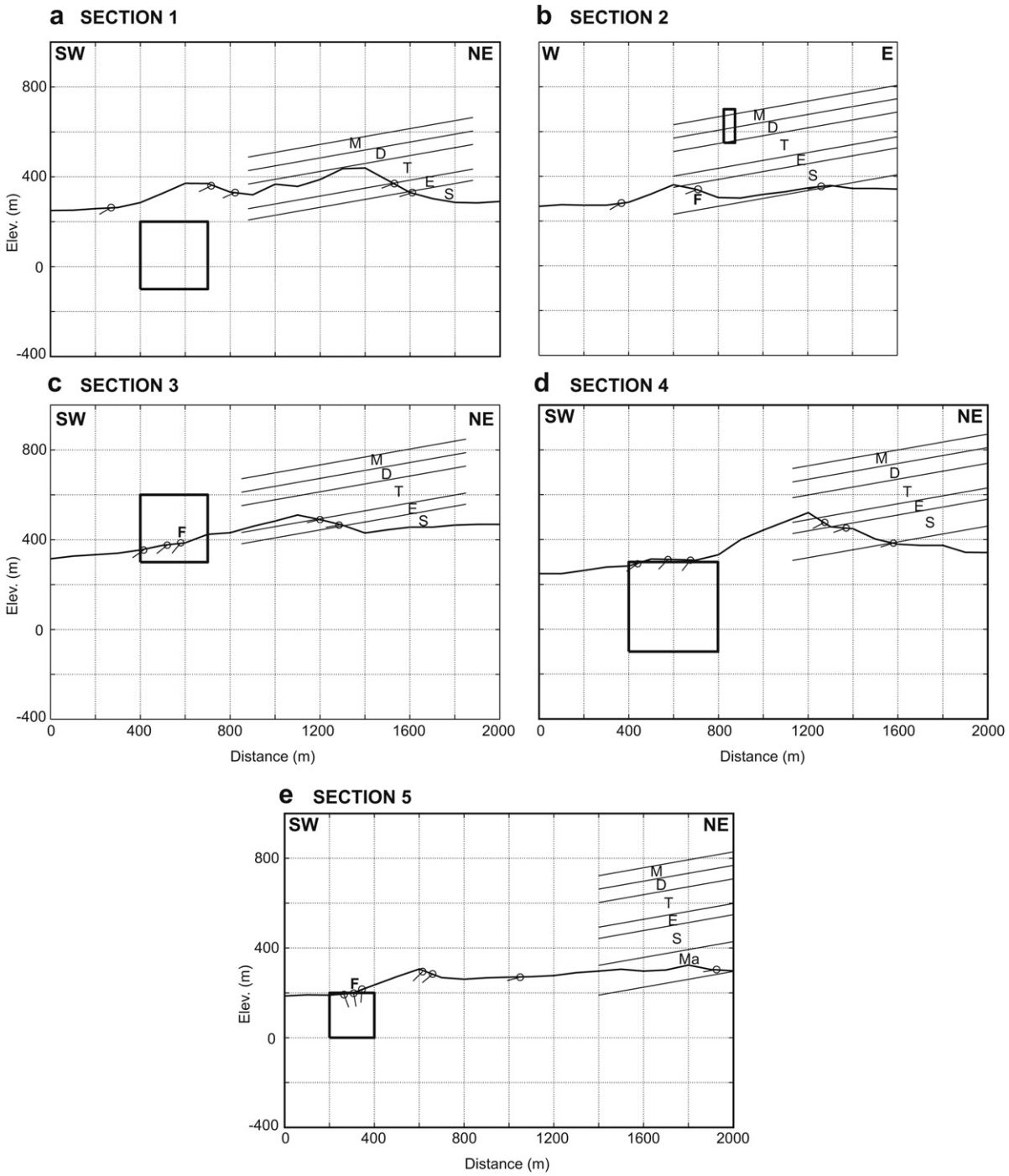

Fig. 8. Bedding data along topographic profiles 1 to 5 in Fig. 7. In each profile, long, parallel lines dipping west are the footwall pre-rift stratigraphic template used to model the profile data. Letters in the templates correspond to M: Mokattam, D: Darat, T: Thebes, E: Esna, S: Sudr, and Ma: Matulla Formations. Short ticks with circles are bedding dips at the contacts shown in the stratigraphic template. The rectangle shows the area where the fault tip was searched. In breached profiles 2, 3 and 5, the letter F shows the approximate surface location of the master fault.

and locally represented by an unbreached monocline (Figs. 7 and 8e). The key feature in this section is the presence of sub-vertical to overturned beds on the monocline limb (Fig. 8e). The four inversions for this profile (Table 1) produce minimum f_{obj} values that are much higher than those for sections 1–4 (Fig. 9). The match between the modeled and measured bedding intersections is not as good in this section as in sections 1–4. The inversions suggest a steep dipping master fault (80°), low P/S (0.75–1.2), low TA (20–40°), and high fault slip (650–750 m). The selected model has low P/S (0.75) and high fault slip (698 m, Table 1, Fig. 10e). It reproduces the location of the monocline limb, but it can only generate moderate to steeply-dipping beds at the location where the fault is breaching. In the field, along section 5, it is observed that the sub-vertical to overturned beds on the monocline limb are linked to westward-verging reverse faults. These structures are not explicitly included in the trishear model. In the field, the reverse

Table 1
Upper and lower limits, initial guesses, and selected models for the inversions of sections 1–5 in Fig. 8. For each **a** vector, the entries correspond to the six parameters of the 2D trishear model: *x* and *y* location of the fault tip, ramp angle, P/S, TA, and fault slip.

Section (Fig. 8)	Lower ($\mathbf{a_{max}}$) and upper ($\mathbf{a_{min}}$) limits	Initial guess ($\mathbf{a_0}$)	P/S variations in initial guess	Selected model ($\mathbf{a_f}$, Fig. 10)
1	$\mathbf{a_{min}}$ = [400 −100 60 1.0 20 100] $\mathbf{a_{max}}$ = [700 200 80 3.0 100 500]	$\mathbf{a_0}$ = [550 50 70 1.5 60 300]	1.5, 1.75, 2.0, 2.25	$\mathbf{a_f}$ = [405 −92 77 1.89 81 182]
2	$\mathbf{a_{min}}$ = [825 550 60 1.0 20 100] $\mathbf{a_{max}}$ = [875 700 80 3.0 100 500]	$\mathbf{a_0}$ = [825 625 70 1.5 60 300]	1.5, 1.75, 2.0, 2.25	$\mathbf{a_f}$ = [837 686 71 1.87 99 377]
3	$\mathbf{a_{min}}$ = [400 300 60 1.0 20 100] $\mathbf{a_{max}}$ = [700 600 80 3.0 100 500]	$\mathbf{a_0}$ = [575 390 70 1.5 60 300]	1.5, 1.75, 2.0, 2.25	$\mathbf{a_f}$ = [589 390 69 1.90 62 355]
4	$\mathbf{a_{min}}$ = [400 −100 60 1.0 20 100] $\mathbf{a_{max}}$ = [800 300 80 3.0 100 500]	$\mathbf{a_0}$ = [600 100 70 1.5 60 300]	1.5, 1.75, 2.0, 2.25	$\mathbf{a_f}$ = [666 46 75 1.43 64 416]
5	$\mathbf{a_{min}}$ = [200 0 60 0.5 20 100] $\mathbf{a_{max}}$ = [400 200 80 3.0 100 750]	$\mathbf{a_0}$ = [300 100 70 1.5 60 500]	1.5, 1.75, 2.0, 2.25	$\mathbf{a_f}$ = [301 198 80 0.75 22 698]

faults detach along ductile mudstone-dominated units (Duwi, Esna and Darat formations) and may be associated with a non-planar, dip-segmented master fault, and/or gravitational sliding along the mudstone-dominated detachment horizons (Whipp, 2011).

The overall scenario suggested by inverse trishear modeling of the Hadahid monocline is that of a fault system decreasing in fault slip from south to north (sections 5 to 1 in Fig. 10); this is consistent with interpretations made from field observations. In addition, the P/S and the initial location of the fault tip (i.e. depth of fault nucleation) appear to vary along strike. The along-strike change from the unbreached Hadahid monocline segment (section 4, Figs. 7 and 10d) to the breached Hadahid fault segment (sections 2

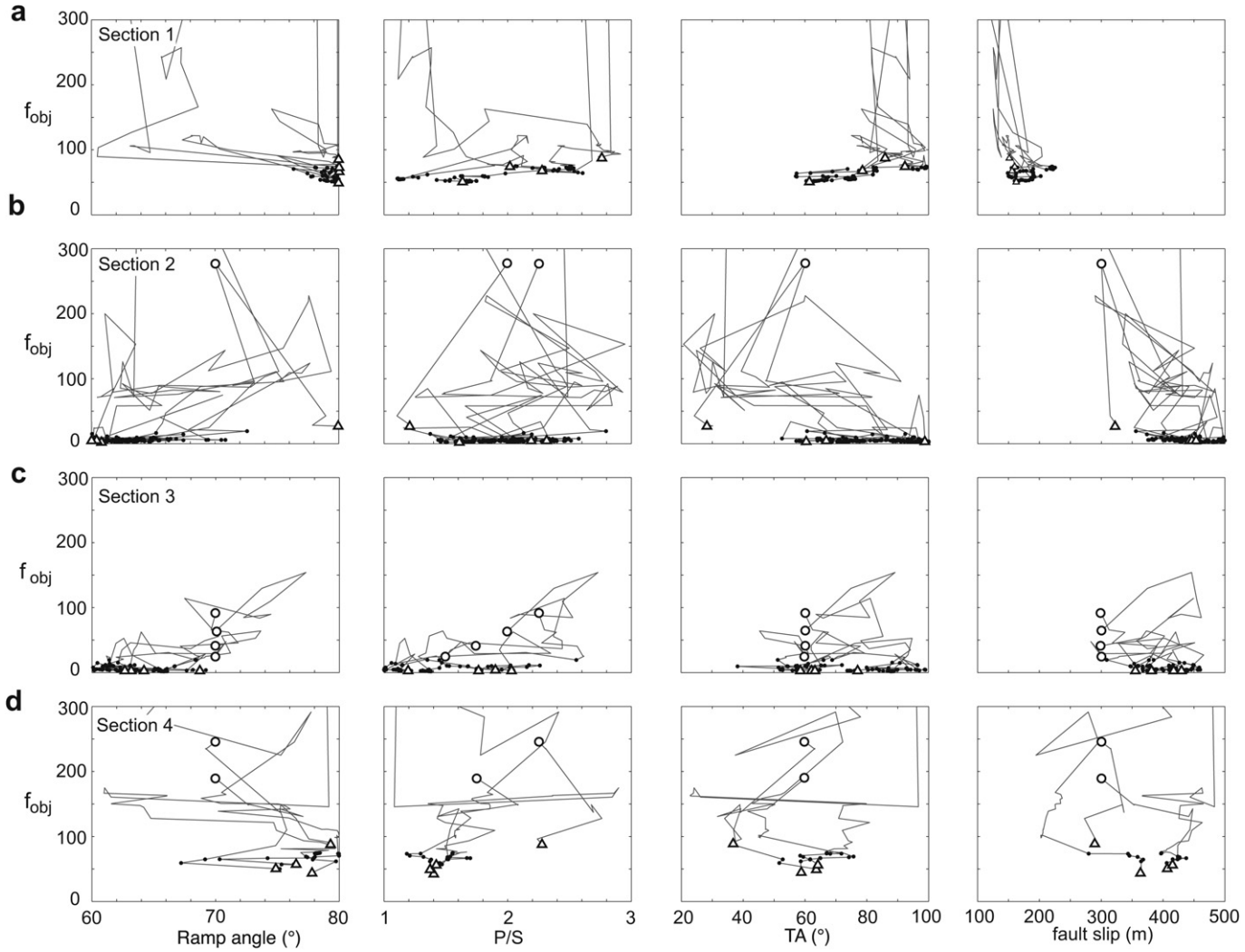

Fig. 9. Evolution of simulated annealing optimizations for the trishear parameters that best restore bedding intersections along the profiles a. 1, b. 2, c. 3, and d. 4 of Fig. 8. The paths of the optimizations are shown on: Ramp angle versus f_{obj} (first column), P/S versus f_{obj} (second column), TA versus f_{obj} (third column), and fault slip versus f_{obj} (fourth column) diagrams. Four optimization paths are shown for each section, each path consisting of 750 iterations. For each path, the circle represents the initial estimate, and the triangle the final iteration. Black dots indicate low f_{obj} ($\leq$75 in a and d, and $\leq$20 in b and c), "possible" models.

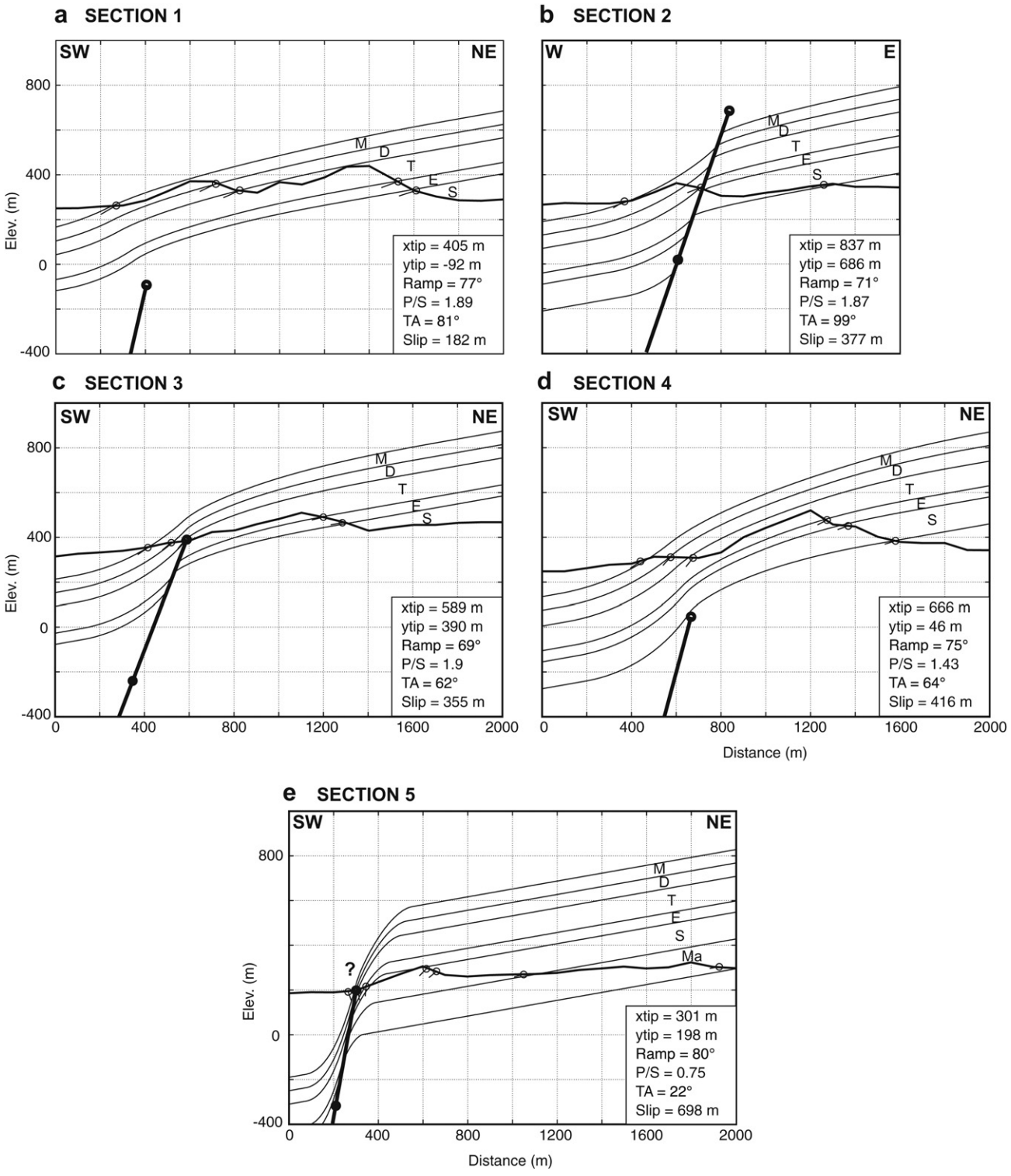

Fig. 10. Selected trishear models for the profile data along sections 1–5 in Fig. 8. In each section, the circles on the modeled fault show the initial (lowermost circle) and final (uppermost circle) location of the fault tip. Inset legend shows the parameters of the selected model. Letters for stratigraphic units are the same as in Fig. 8.

and 3, Figs. 7 and 10b,c) is explained by a higher P/S and progressively shallower initial fault tip in the Hadahid fault segment. At the northern termination of the HFS, the Feiran segment (section 1, Figs. 7 and 10a) is associated with low fault slip, ca. 50% of that in the Hadahid fault segment to the south (sections 2 and 3, Figs. 7 and 10b,c). Inverse trishear modeling suggests that the along-strike variability of the Hadahid monocline is controlled by along-strike variations in fault displacement, P/S and depth of fault nucleation. With the available data, however, it is not possible to arrive at a unique trishear model for the monocline (e.g. section 3 can be fit by low P/S and shallow initial fault tip, or vice-versa, Fig. 9c). In addition, rock material-related parameters, such as P/S and TA,

were kept constant in the inversion. These parameters were more likely to vary during fold growth in response to vertical and lateral changes in mechanical stratigraphy. Additional parameters such as the concentration factor (Zehnder and Allmendinger, 2000), which describe the heterogeneity of the trishear zone, were not considered in the search. The results of the inversions should thus be considered as an approximation of the overall geometry and evolution of the monocline.

4. Spread of possible models

An interesting outcome of this analysis is the significance of the spread of trishear parameter values in the "possible" models. Are there some parameters that show more spread or variability than others? The inversion of the Shijia trench site shows that in the possible models there is significant spread in fault slip, TA, and P/S, with the spread in P/S being lower than that in TA (Fig. 4). The spread in fault slip is explained by the fact that, with the exception of some areas in the backlimb of the anticline, most of the outcrop lies within the folded region (Figs. 2b and 6) and there are not many points in the hanging wall and footwall areas to constrain fault slip. The lower spread in P/S than in TA has been observed in inverse modeling of synthetic, thrust-associated trishear models (Allmendinger et al., 2004 and Fig. 1b). Trishear fold geometries are more sensitive to changes in P/S than in TA (Fig. 1b). A physically satisfying result since of the six trishear-parameters, it is the P/S the one we can relate to rock properties (high P/S in more competent rocks and vice-versa, Allmendinger et al., 2004). Trishear inverse modeling of the HFS indicates that fault slip is well constrained, but there is significant spread in P/S and TA, with the spread in P/S being lower than that in TA (Fig. 9). The low variability in fault slip is explained by the fact that a large portion of the beds is in the backlimb of the footwall anticline (Figs. 8 and 10). These unfolded beds provide a fixed template for the trishear model, thus constraining fault slip. A critical piece of information that is lacking and that would help to further constrain the slip of the master fault is the location of bedding in the hanging wall west of the HFS. Similar to the Shijia trench example, the lower variability of P/S with respect to TA (Fig. 9) confirms the greater importance of P/S in the inversion.

Another question is how the spread of trishear parameter values in the possible models changes with fold evolution? Is the spread of the possible parameter values constant, or does it change through time with fold growth? We can attempt to answer this question by looking at the modeling results of the Hadahid monocline (Fig. 9) because to a certain extent, the along strike, spatial variability of the Hadahid monocline reflects different stages of its temporal evolution (Gawthorpe et al., 1997; Sharp et al., 2000; Whipp, 2011). However, possible along-strike changes of P/S and depth of fault nucleation (Fig. 10), the effects of mechanical stratigraphy, and the incompleteness of the dataset make difficult to establish in this structure the variation of the possible parameter values with fold growth. In an attempt to answer this question, we ran simulated annealing, trishear inversions of four sequential stages in the evolution of a clay model of an extensional forced fold (Withjack et al., 1990). The clay in the model is homogenous, and the slip of the master fault and fold geometry throughout the evolution of the structure are known (Fig. 11). The clay model is therefore an ideal case to study the variation in the spread of possible trishear models with fold growth.

Fig. 12 shows the results of the simulated annealing inversions for the trishear parameters that best restore one of the key marker beds within the model (marker bed indicated with arrows in Fig. 11) at four stages of the fold's evolution. The paths of the optimizations are shown for the ramp angle, P/S, TA and fault slip (Fig. 12). The extent of the search of these parameters in the inversions correspond to the parameter ranges shown in Fig. 12, and for the fault tip location, it is defined by the rectangular areas

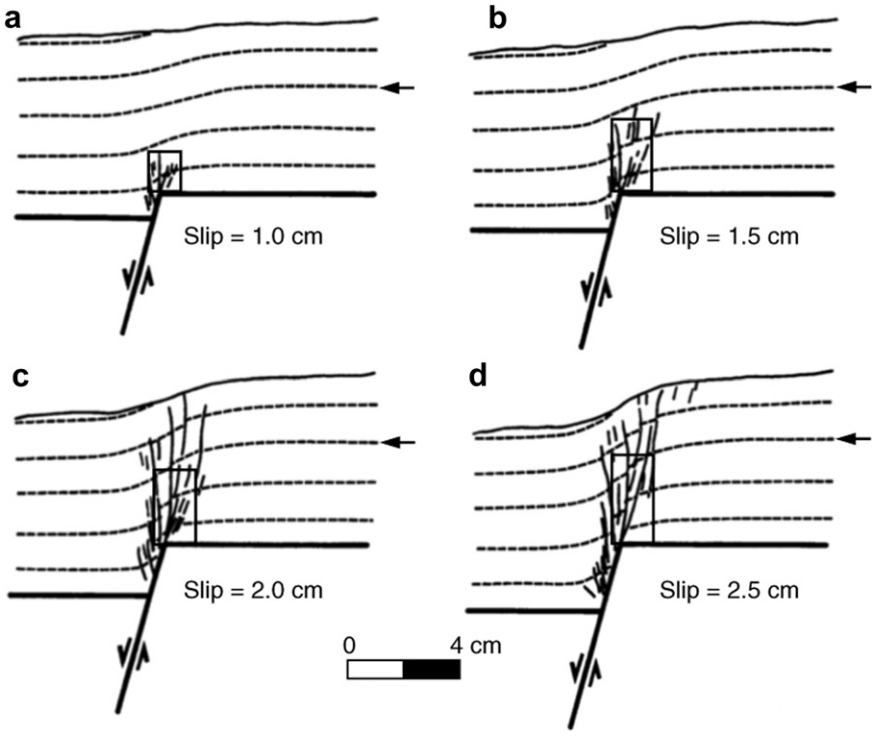

Fig. 11. Four stages in the evolution of a homogenous clay model of an extensional forced fold produced by a 75° dipping normal fault. Displacement on master normal fault are a. 1.0, b. 1.5, c. 2.0, and d. 2.5 cm. Dashed lines are markers that record fold shape. Thin, solid lines are secondary normal and reverse faults. Arrows show the marker used in the inversions. Rectangles show the areas where the final location of the fault tip was searched. Modified from Fig. 6 of Withjack et al. (1990).

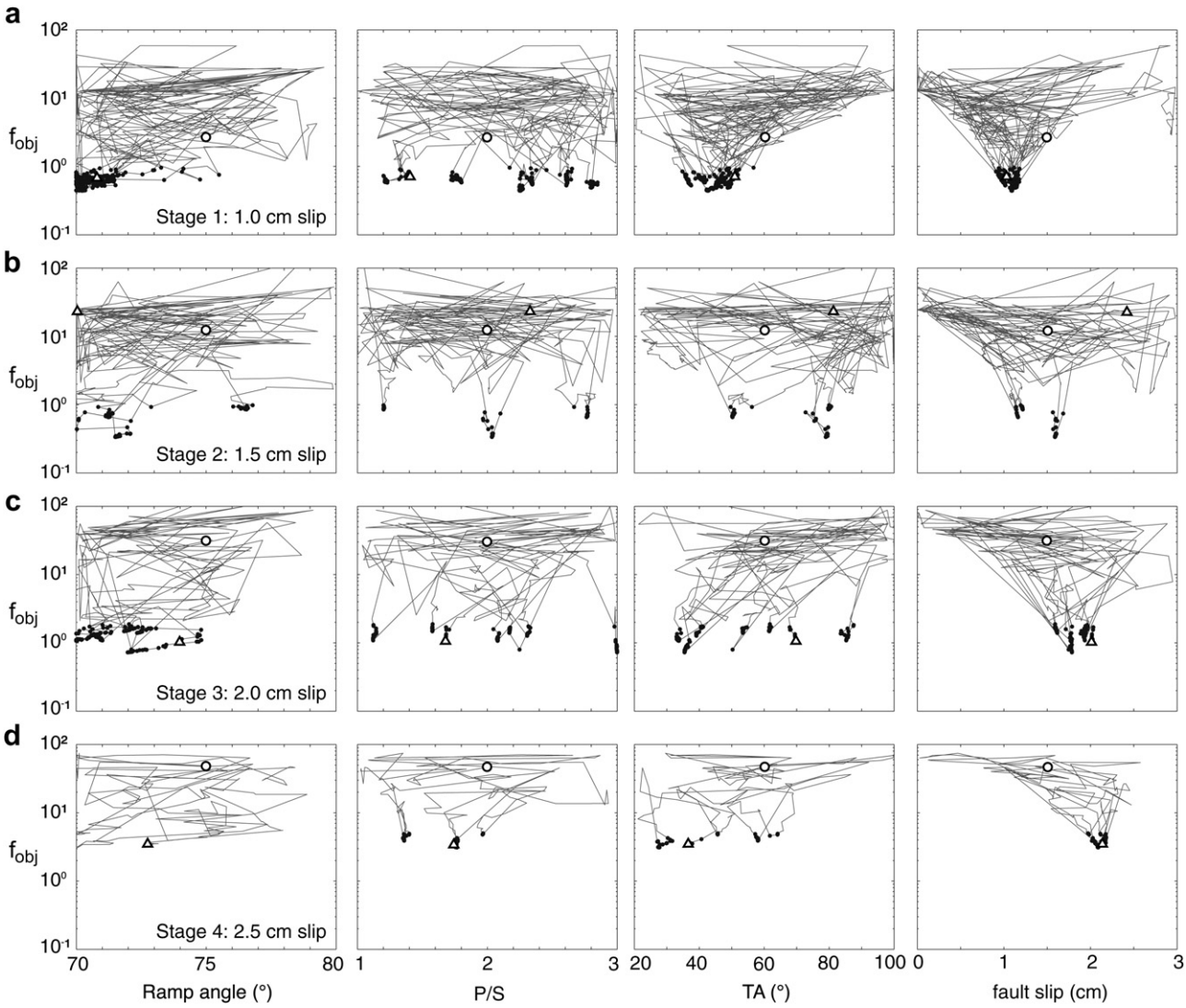

Fig. 12. Evolution of simulated annealing optimizations for the trishear parameters that best restore the third marker of the clay model (Fig. 11, arrows), at four stages corresponding to master normal fault displacements of a. 1.0, b. 1.5, c. 2.0, and d. 2.5 cm. The paths of the optimizations are shown on: Ramp angle versus f_{obj} (first column), P/S versus f_{obj} (second column), TA versus f_{obj} (third column), and fault slip versus f_{obj} (fourth column) diagrams. A total of 2000 iterations were used in each optimization. In each plot, the circle represents the initial estimate, and the triangle the final iteration. Black dots indicate low f_{obj} ($\leq$1 in a and b, $\leq$2 in c, and $\leq$5 in d), "possible" models. Notice that the vertical f_{obj} axis is logarithmic.

shown in Fig. 11. A total of 2000 iterations were used in each inversion. Circles and triangles in Fig. 12 show the initial estimate and final iteration, respectively. For the inversion of the marker at an early stage (slip of master fault = 1.0 cm, Fig. 11a), the solution is well constrained in TA (40–50°) and fault slip (1.0–1.1 cm), but not in ramp angle (70–75°) and P/S (1.25–2.75, Fig. 12a). At a later stage (slip of master fault = 1.5 cm, Fig. 10b), the solution is well constrained in fault slip (1.6 cm), but not as much in TA (50–70°). Compared to the first stage, the solution is more constrained in ramp angle and P/S with the lowest f_{obj} values around 72° and 2.0, respectively (Fig. 12b). For stage 3 (slip of master fault = 2.0 cm, Fig. 11c), the solution is well constrained in slip (1.9–2.0 cm), and better constrained in ramp angle (73–75°) and P/S (1.75–2.25), than in TA (40–80°, Fig. 12c). For the last stage (slip of master fault = 2.5 cm, Fig. 11d), the solution is well constrained in fault slip (2.1–2.2 cm) and to a certain extent in P/S (1.75–2.0), but not as much in ramp angle (70–77°) and TA (30–70°, Fig. 12d). At this stage, the minimum f_{obj} values are much higher (i.e. worse fits) than in the previous steps. This is because the marker is offset by secondary faults (Fig. 11d). These secondary faults are predicted by the trishear model (e.g. Allmendinger, 1998, his Fig. 9), but in trishear they are just passive lines that don't offset the beds.

Two important conclusions can be drawn from this exercise. The first one is that the solution for fault slip is highly constrained by including hanging wall and footwall bedding areas outside the fold. If that is the case, the predicted slip is close to that of the master fault (a conclusion that is applicable to the Hadahid monocline trishear inversion). As the fold grows and the beds become more discontinuous, the predicted fault slip departs from the slip of the master fault (compare Fig. 12c–d). The second conclusion is that the P/S seems to be a parameter that characterizes the evolution of the deformation than the TA. At early folding stages (stage 1 in clay model) the resolved P/S shows high variability, but at some point (e.g. stage 2 in clay model) a preferred P/S value can be established (around 2.0 in the clay model), and P/S predictions for later stages are concentrated around this value (although there is a lower possibility for end, low or high P/S values, Fig. 12). The predicted TA on the other hand varies significantly through fold evolution, with the exception

of early folding stages when the folded area is narrow and the TA has small values (Fig. 12). The P/S seems to be more related to an inherent property such as rock mechanical behavior (e.g. clay properties in the analog model of Fig. 11), than the TA, which seems to be more influenced by the evolution of fold geometry.

5. Discussion

We have shown the application of a robust and efficient simulated annealing algorithm to trishear inverse modeling. The algorithm effectively traverses the parameter space in search for local minima, without being trapped in the minima, and thereby samples more possible solutions globally. The aim of the inversion is not to find the "best-fit" model, but rather the "range" of models that can fit the structure; the examples shown in this paper illustrate this philosophy. Example 1 from the Shijia trench site, Taiwan, where a contractional fault-propagation fold is developed, shows that even for a highly complete fold dataset with low uncertainties in acquisition and interpretation, it is possible to fit a range of models to the data. Example 2 from the Hadahid monocline, Egypt, where an extensional fault-propagation fold is developed, shows that for the more common case of an incomplete dataset with higher uncertainties, it is possible to use the algorithm to evaluate a range of models that can fit the data, thus avoiding biases in the interpretation. In both cases, a threshold value (i.e. a minimum value of f_{obj}) is used to separate possible models. The selection of this value is influenced by the uncertainties in the data, as well as the suitability of the model to reproduce the processes that created the structure (e.g. secondary thrusting in the Hadahid monocline).

The modeling technique discussed in this paper provides critical insights into the controls on the geometry and evolution of fault-propagation folds in contractional and extensional settings. The inversions of the natural and analog examples show that the spread of the trishear parameters that can possibly fit a structure is not only influenced by the uncertainty of the data and the suitability of the model, but also by the evolution of the structure and the mechanical behavior of the folded rocks. Of the parameters controlling the evolution of the trishear model, it is the P/S that seems more related to the mechanical behavior of the rocks being folded. The TA, on the other hand, varies considerably during fold growth (Fig. 12). These conclusions are also supported by mechanical, discrete element modeling of fault-propagation folds (Hardy and Finch, 2006).

Structural modeling is not a problem with a unique answer. Besides dealing with data uncertainties (e.g. Cardozo and Aanonsen, 2009), the modeler has to be aware that the data can be fit by more than one model scenario (i.e. combination of model parameters). Structural modeling today concentrates on getting a valid interpretation that we know is not unique. However, the statistical significance of this interpretation and its uniqueness are rarely evaluated, although Judge and Allmendinger (2011) have recently described a technique to assess uncertainty in balanced cross sections. The methodology described in our paper is a step forward toward a more holistic approach in structural modeling. This approach acknowledges the impact of uncertainty and, rather than providing a precise representation of the data, gives an estimation of the possible models that can fit the data and their uncertainties. Such an approach can be extended to any inverse structural problem involving kinematic or even mechanical modeling. Today, computer speed and improved modeling algorithms make this possible.

Acknowledgments

We would like to thank Sigurd Aanonsen, Rob Gawthorpe, and Ian Sharp for discussions on fault related folding and inverse problems. Sigurd Aanonsen suggested the use of the simulated annealing algorithm to trishear inverse modeling. Paul Whipp thanks Statoil and EPSRC for funding his Ph.D. research in the Hadahid, Gulf of Suez area. Comments by Richard Groshong and an anonymous reviewer improved the manuscript. The algorithm was implemented in MATLAB® using the MATLAB Global Optimization Toolbox™. The scripts are available at the web page: http://homepage.mac.com/nfcd/work/matlabScripts.html.

References

Allmendinger, R.W., 1998. Inverse and forward numerical modeling of trishear fault-propagation folds. Tectonics 17, 640–656.
Allmendinger, R.W., Shaw, J.H., 2000. Estimation of fault propagation distance from fold shape: implications for earthquake hazard assessment. Geology 28, 1099–1102.
Allmendinger, R.W., Zapata, T.R., Manceda, R., Dzelalija, F., 2004. Trishear kinematic modeling of structures, with examples from the Neuquén Basin, Argentina. In: McClay, K.R. (Ed.), Thrust Tectonics and Hydrocarbon Systems, vol. 82. American Association of Petroleum Geologists Memoir, pp. 356–371.
Cardozo, N., 2005. Trishear modeling of fold bedding data along a topographic profile. Journal of Structural Geology 27, 495–502.
Cardozo, N., 2008. Trishear in 3D. Algorithms, implementation, and limitations. Journal of Structural Geology 30, 327–340.
Cardozo, N., Aanonsen, S., 2009. Optimized trishear inverse modeling. Journal of Structural Geology 31, 546–560.
Cardozo, N., Allmendinger, R.W., Morgan, J.K., 2005. Influence of mechanical stratigraphy and initial stress state on the formation of two fault propagation folds. Journal of Structural Geology 27, 1954–1972.
Champion, J., Mueller, K., Tate, A., Guccione, M., 2001. Geometry, numerical models and revised slip rate for the Reelfoot fault and trishear fault-propagation fold, New Madrid Seismic Zone. Engineering Geology 62, 31–49.
Chen, W.S., Huang, B.S., Chen, Y.G., Lee, Y.H., Yang, C.N., Lo, C.H., Chang, H.C., Sung, Q.C., Hiang, N.W., Lin, C.C., Sung, S.H., Lee, K.J., 2001. 1999 Chi–Chi earthquake: a case study on the role of thrust-ramp structures for generating earthquakes. Bulletin of the Seismological Society of America 91, 986–994.
Chen, Y.G., Lai, K.Y., Lee, Y.H., Suppe, J., Chen, W.S., Lin, Y.N., Wang, Y., Hung, J.H., Kuo, Y.T., 2007a. Coseismic fold scarps and their kinematic behavior in the 1999 Chi–Chi earthquake Taiwan. Journal of Geophysical Research 112, B03S02. doi:10.1029/2006JB004388.
Chen, W.S., Lee, K.J., Lee, L.S., Streig, A.R., Chang, H.C., Lin, C.W., 2007b. Paleoseismic evidence for coseismic growth-fold in the 1999 Chi–chi earthquake and earlier earthquakes, central Taiwan. Journal of Asian Earth Sciences doi:10.1016/j.jseaes.2006.07.027.
Corfield, S., Sharp, I.R., 2000. Structural style and stratigraphic architecture of fault propagation folding in extensional settings: a seismic example from the Smørbukk area, Halten Terrace, Mid-Norway. Basin Research 12, 329–341.
Erslev, E.A., 1991. Trishear fault-propagation folding. Geology 19, 617–620.
Erslev, E.A., Mayborn, K.R., 1997. Multiple geometries and modes of fault-propagation folding in the Canadian thrust belt. Journal of Structural Geology 19, 321–335.
Ferrill, D.A., Morris, A.P., Sims, D.W., Waiting, J.D., Hasegawa, S., 2005. Development of synthetic layer dip adjacent to normal faults. In: Sorkhabi, R., Tsuji, Y. (Eds.), Faults, Fluid Flow, and Petroleum Traps, vol. 85. AAPG Memoir, pp. 125–138.
Finch, E., Hardy, S., Gawthorpe, R., 2003. Discrete element modeling of contractional fault-propagation folding above rigid basement fault blocks. Journal of Structural Geology 25, 515–528.
Finch, E., Hardy, S., Gawthorpe, R., 2004. Discrete-element modelling of extensional fault-propagation folding above rigid basement fault blocks. Basin Research 16, 489–506.
Gawthorpe, R., Hardy, S., 2002. Extensional fault propagation folding and base-level change as controls on growth strata geometries. Sedimentary Geology 146, 47–56.
Gawthorpe, R.L., Sharp, I., Underhill, J.R., Gupta, S., 1997. Linked sequence stratigraphic and structural evolution of propagating normal faults. Geology 25, 795–798.
Hardy, S., Finch, E., 2006. Discrete element modelling of the influence of cover strength on basement-involved fault-propagation folding. Tectonophysics 415, 225–238.
Hardy, S., Ford, M., 1997. Numerical modelling of trishear fault-propagation folding. Tectonics 16, 841–854.
Hardy, S., McClay, K., 1999. Kinematic modelling of extensional fault-propagation folding. Journal of Structural Geology 21, 695–702.
Judge, P., Allmendinger, R.W., 2011. Assessing uncertainties in balanced cross sections. Journal of Structural Geology 33, 458–467.
Lin, M.L., Wang, C.P., Chen, W.S., Yang, C.N., Jeng, F.S., 2007. Inference of trishear-faulting processes from deformed pregrowth and growth strata. Journal of Structural Geology 29, 1267–1280.
The MathWorks Inc. MATLAB Global Optimization Toolbox ™ 3 User's Guide. 2010. Available at: http://www.mathworks.com/access/helpdesk/help/pdf_doc/gads/gads_tb.pdf.

Moustafa, A.R., 1987. Drape folding in the Baba-Sidri area, eastern side of the Suez rift, Egypt. Journal of Geology 31, 15–27.
Moustafa, A.R., 2004. Geologic Maps of the Eastern Side of the Suez Rift (Western Sinai Peninsula), Egypt. American Association of Petroleum Geologists/Datapages, Inc.. GIS Series (Geologic maps and cross sections in digital format on CD).
Moustafa, A.R., El-Raey, A.K., 1993. Structural characteristics of the Suez rift margins. Geologische Rundschau 82, 101–109.
Patton, T.L., Moustafa, A.R., Nelson, R.A., Abdine, S.A., 1994. Tectonic evolution and structural setting of the Suez Rift. In: Landon, S.M. (Ed.), Interior Rift Basins, vol. 59. American Association of Petroleum Geologists Memoir, pp. 7–55.
Sharp, I.R., Gawthorpe, R.L., Underhill, J.R., Gupta, S., 2000. Fault propagation folding in extensional settings: examples of structural style and synrift sedimentary response from the Suez rift, Sinai, Egypt. Geological Society of America Bulletin 112, 1877–1899.
Shaw, J.H., Shearer, P.M., 1999. An elusive blind-thrust fault beneath metropolitan Los Angeles. Science 283, 1516–1518.
Whipp, P.S., 2011. Fault propagation folding and the growth of normal faults. Ph.D. thesis. Imperial College, London.
Withjack, M.O., Olson, J., Peterson, E., 1990. Experimental models of extensional forced folds. American Association of Petroleum Geologists Bulletin 74, 1038–1054.
Yue, L.F., Suppe, J., Hung, J.H., 2005. Structural geology of a classic thrust belt earthquake: the 1999 Chi–Chi earthquake Taiwan (Mw = 7.6). Journal of Structural Geology 27, 2058–2083.
Zehnder, A.T., Allmendinger, R.W., 2000. Velocity field for the trishear model. Journal of Structural Geology 22, 1009–1014.